A prediction model for the failure threshold in a CoNiV medium-entropy alloy *⊙*

Rong Hao 💿 ; Guanhao Liu 💿 ; Zhong Wang 💿 ; Huijun Yang 💌 💿 ; Peter K. Liaw 💿 ; Junwei Qiao 💌 💿



J. Appl. Phys. 134, 135101 (2023) https://doi.org/10.1063/5.0158721





Articles You May Be Interested In

Statistical analysis of serrated flows in CoNiV medium-entropy alloy

Appl. Phys. Lett. (February 2024)

Pressure-driven structural transition in CoNi-based multi-principal element alloys

Appl. Phys. Lett. (August 2023)

Quasi-superplasticity in the AlCoNiV medium entropy alloy with Heusler L2₁ precipitates

APL Mater. (November 2022)

Challenge us.

What are your needs for periodic signal detection?



Find out more

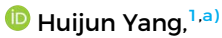




A prediction model for the failure threshold in a CoNiV medium-entropy alloy

Cite as: J. Appl. Phys. 134, 135101 (2023); doi: 10.1063/5.0158721 Submitted: 17 May 2023 · Accepted: 14 September 2023 ·

Published Online: 2 October 2023







AFFILIATIONS

- Laboratory of High-Entropy Alloys, College of Materials Science and Engineering, Taiyuan University of Technology, Taiyuan 030024, China
- ²Department of Materials Science and Engineering, The University of Tennessee, Knoxville, Tennessee 37996-2200, USA
- ³Key Laboratory of Interface Science and Engineering in Advanced Materials, Ministry of Education, Taiyuan University of Technology, Taiyuan 030024, China

ABSTRACT

Portevin-Le Chatelier effect, associated with dynamic strain aging, is widely found in various alloys, and the maximum serration magnitude from the tensile stress-strain curve can be considered as the point closest to the failure threshold. Due to the difficulty to define solute and \(\preceq \) solvent atoms in multicomponent alloys, it is a great challenge to explore the serration mechanism. In this study, the atoms that play the $\frac{9}{8}$ role of pinning are defined as solute atoms. Aided by mean-field theory, an *in situ* pinning model coupled with the twinning effect in a $\frac{9}{8}$ CoNiV alloy with low stacking fault energies is successfully established, which can well predict the failure threshold, i.e., the maximum serration magnitude. The present study paves a new way to correlate the serration dynamics and *in situ* pinning, and further predicts the failure threshold upon loading for multicomponent high- and medium-entropy alloys.

Published under an exclusive license by AIP Publishing. https://doi.org/10.1063/5.0158721

I. INTRODUCTION

The serrated flow generally appears in the materials, reflecting the fluctuation of the intrinsic structural parameters of the materials under the action of external loadings. It is specifically manifested as the zigzag fluctuations of the plastic flows on the stress-strain curves.2 This phenomenon indicates the plasticity instability of the materials upon loading, which is not conducive to the mechanical properties, and it brings great challenges to the performance prediction. In crystalline alloys, the serrated flows are usually called the Portevin-Le Chatelier (PLC) effect,^{3,4} which is considered to be the cyclic process of the pinning and unpinning of mobile dislocations by the solute atoms. This process is also called the dynamic strain aging effect.5-

As a novel kind of emerging crystalline alloys, high-entropy alloys (HEAs)⁸⁻¹⁵ have received wide attention for their excellent properties. Usually, the alloys whose configuration entropy is between 1R and 1.5R are called medium-entropy alloys (MEAs), while those whose configuration entropy is greater than 1.5R are called high-entropy alloys. 16 Broadly speaking, both MEAs and HEAs can be collectively referred to be multi-principal alloys.

Due to the complex interactions between highly concentrated elements and dislocations in multicomponent HEAs, 17,18 it brings great difficulty to explore the serration mechanisms. Though Tirunilai et al. 19 suggested that LC locks may be the origin of serrations generation, and Naeem et al. 20,21 explored the deformation behavior of HEA at low temperatures, the serration mechanism associated with plastic instability at high temperatures is still not fully resolved. The serration flows in conventional alloys is often attributed to repeated pinning and depinning of mobile dislocations by solute atoms or precipitates.²² In contrast, a sluggish diffusion may exist in HEAs,²³ and thus, the diffusion speed of solute atoms is insufficient to complete the pinning of the mobile dislocations. Tsai et al.²⁴ proposed a mechanism for in situ pinning through calculating the time for atoms to diffuse and pin dislocations during *in situ* pinning.²⁵ It is proved that a high diffusion rate in any direction in the dislocation nucleus surrounding the strain sources leads to rapid pinning by forming the segregation or atmosphere rich in solute atoms. Although Yang et al. 26 introduced the concept of "mysterious solutes," the definition of solute atoms in HEAs remains challenging.

^{a)}Authors to whom correspondence should be addressed: pineyang@126.com and qiaojunwei@gmail.com

In the present work, we try to explore the serration mechanisms in the CoNiV MEA in detail at different temperatures and strain rates. Combined the statistical analysis of stress serrations with the mean-field theory, ²⁷ the maximum serration amplitude under different temperatures can be calculated. The dynamic strain aging time was calculated to predict the strain associated with the failure threshold, by establishing an *in situ* pinning model.

II. EXPERIMENTAL PROCEDURE

The CoNiV equiatomic alloy was fabricated in a vacuum arc melting furnace under argon atmosphere. Ingots were homogenized at 1100 °C for 2 h and cold-rolled to a 75% thickness reduction from 5 to 1.25 mm. The cold-rolled plates with a 1.25 mm thickness were annealed at 950 °C for 1 h and then water-quenched. Uniaxial tensile tests were conducted, employing a universal testing machine (Instron 5969) at 300, 350, and 400 °C, at the strain rates of 5×10^{-4} and 1×10^{-3} s⁻¹, and the data-acquisition rate is 500 Hz. The crystal structure was characterized by the x-ray diffraction (Panalytical Aeris), with the Co $K\alpha$ radiation at a scan rate of 2 deg min⁻¹ and a scan step size of 0.02 deg. The microstructures were examined, using a transmission electron microscope (TEM,

JEM-F200) and a scanning electron microscope (SEM, Pheon XL) equipped with an energy dispersive spectrometer (EDS).

III. RESULTS AND DISCUSSION

Figures 1(a) and 1(b) show the tensile stress-strain curves for the CoNiV MEAs under different temperatures at strain rates of 5×10^{-4} and 1×10^{-3} s⁻¹, respectively. Figure 1(c) shows the tensile stress-strain curves at different strain rates at 400 °C. For a better view, the curves are deliberately shifted along the ordinate axis. It is obvious that the serrations are found at different stress-strain curves, and the serration type varies with the temperature and strain rates. At the strain rate of 5×10^{-4} s⁻¹, the stress-strain curve at 300 °C shows a type A serration (type A indicating a periodic upward serration). When the temperature rises to 350 and 400 °C, the serrations change from type A to type B and C serrations (types B and C corresponding to upward and downward serrations, respectively). At 400 °C, as the strain rate decreases from 1×10^{-2} to 5×10^{-4} s⁻¹, the serrations type also changed from type A to type B and C. [The identification basis of the above serrations types is given according to Fig. 1(d)].²⁸ These trends are well consistent with the traditional PLC effect. The x-ray diffraction (XRD)

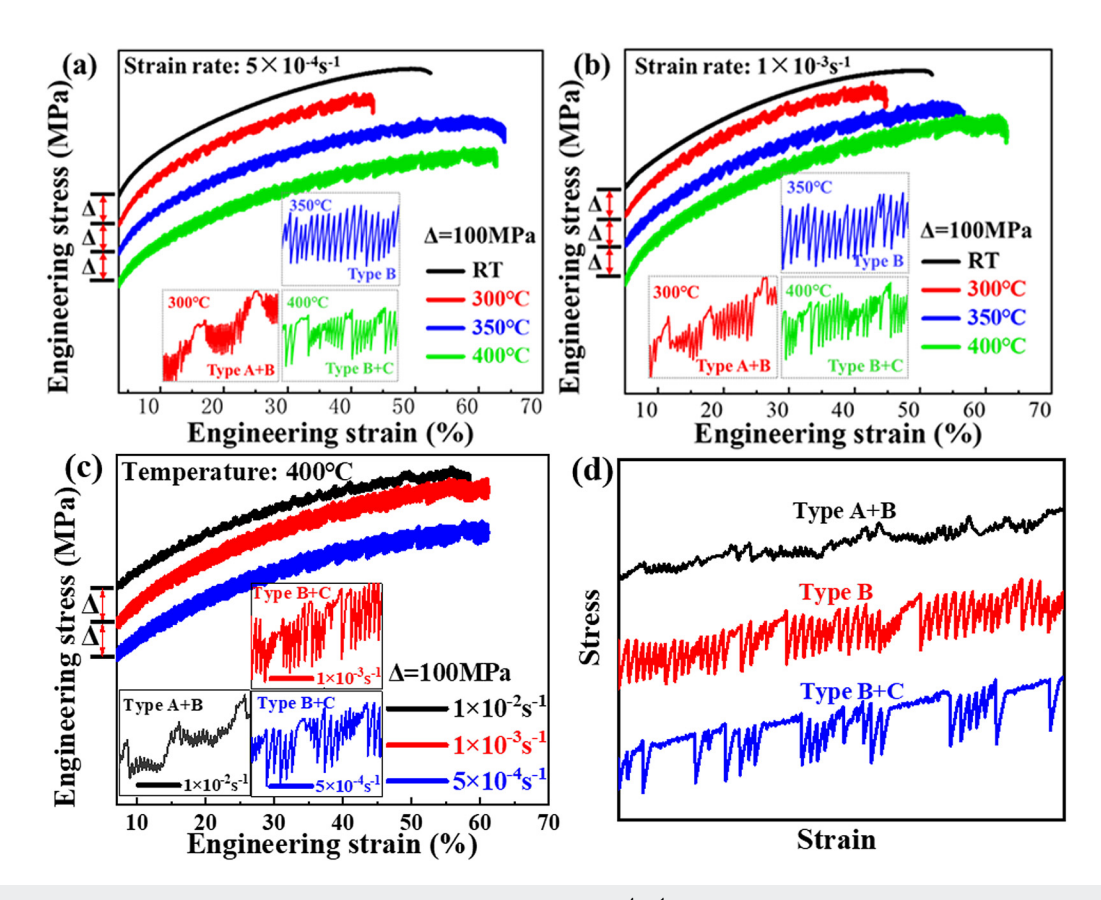


FIG. 1. (a) Tensile stress-strain curves at different temperatures with a strain rate of 5 × 10⁻⁴ s⁻¹; (b) tensile stress-strain curves at different temperatures with a strain rate of 1 × 10⁻³ s⁻¹, (c) tensile stress-strain curves at different strain rates at 400 °C, (d) the profiles corresponding to the three types of serrations. ²⁸

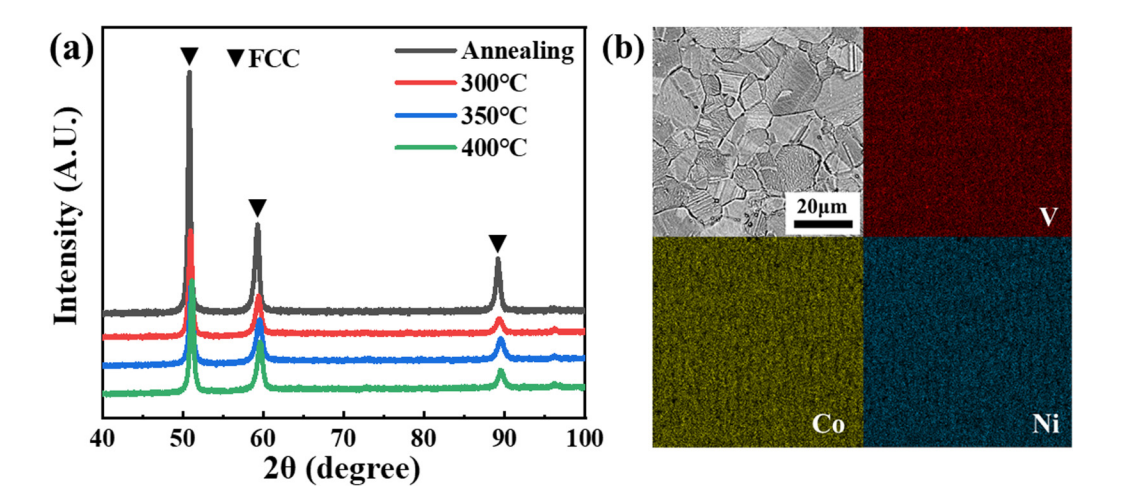


FIG. 2. (a) XRD analysis results before and after the tensile test, (b) scanning electron micrograph (SEM) of CoNiV high-entropy alloy after rolling and annealing and the energy dispersive spectroscopy map of each element.

patterns in Fig. 2(a) revealed the CoNiV MEA with an FCC single phase. Figure 2(b) displays the recrystallized microstructures of the CoNiV MEA. A small number of annealing twins are presented, and the distribution of chemical elements was found to be uniform, as demonstrated in elemental-mapping images.

Figure 3 shows that both the average serration amplitude and the maximum serration amplitude increase with the increase of the temperature, but the average serration amplitude increases greatly. Figure 4(a) indicates that the serration amplitude increases significantly with the increase of the strain, and the fracture occurs after the maximum serration. Therefore, it is of great engineering significance to predict the amplitude and strain corresponding to the occurrence of the maximum serration for a material.

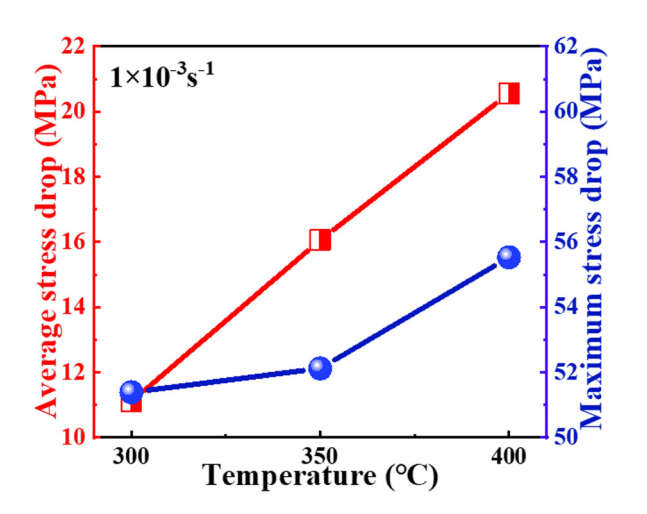


FIG. 3. The average and maximum stress drop vary with temperature at a strain rate of $1 \times 10^{-3} \text{ s}^{-1}$

Considering the long-range dislocation interaction, the barrier interactions between dislocations and solute atoms, and the temperature effects, etc., the flow stress after yielding can be expressed as follows:25

$$\sigma = \sigma_{\varepsilon} + \sigma_{srs} + \sigma_{dsa} - \sigma_{s}$$

$$= \sigma_{0} + h\varepsilon^{m} + s_{in}\ln(\dot{\varepsilon}/\dot{\varepsilon}') + \sigma_{dsa} - \nu(\Delta T/T_{0})^{r}$$

$$\dot{\sigma}_{dsa} = -c_{1}\dot{\varepsilon}\sigma_{dsa} + c_{2}\{\exp[(M - \sigma_{dsa})/c_{3}] - 1\},$$
(2)

$$\dot{\sigma}_{dsa} = -c_1 \dot{\varepsilon} \sigma_{dsa} + c_2 \{ \exp[(M - \sigma_{dsa})/c_3] - 1 \}, \tag{2}$$

where σ_{ε} is the long-range dislocation interaction stress, σ_{srs} is the instantaneous response stress corresponding to the rate change, σ_{dsa} is the interaction stress between the solute atoms and moving dislocations, σ_s is the temperature-related stress, σ_0 is the initial internal stress of the materials, that is, the yield strength, ε is the tensile engineering strain, s_{in} is the instantaneous strain-rate sensitivity coefficient, $\dot{\varepsilon}$ is the instantaneous strain rate, ν is the thermalsoftening coefficient, ΔT is the change of temperature, T_0 is the difference between the melting point and ambient temperature, and h, m, r, c_1 , c_2 , M, and c_3 are constants here.

 $h\varepsilon^m$ can be obtained by approximately fitting (see the supplementary material). Substituting the strain change corresponding to a single stress drop, the maximum stress drop caused by straining can be approximately calculated. It indicates that the maximum stress drop due to strain changes is only about 0.02 MPa, which can be ignored. Considering that the initial internal stress of the materials remains unaltered, and the temperature-affected stress change is less than 0.01 MPa, only the effect of the instantaneous strain rate should be considered to predict the magnitude of the stress drop. From Eq. (1), the stress drop can be obtained as

$$\Delta \sigma = 2s_{in} \ln(\dot{\varepsilon}_1/\dot{\varepsilon}_2) + 2\Delta \sigma_{dsa},\tag{3}$$

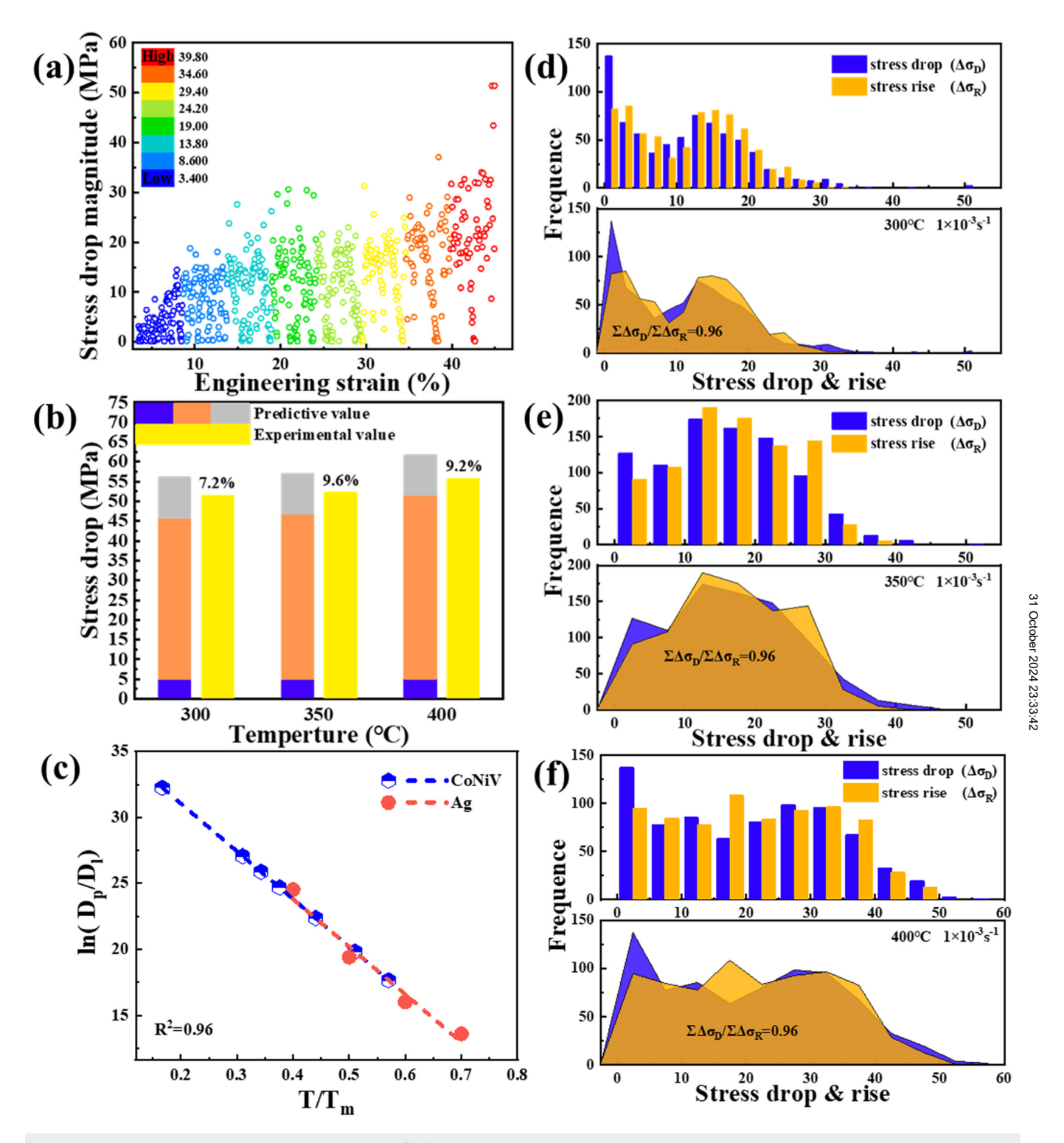


FIG. 4. (a) Variation of serration amplitude with strain at $1 \times 10^{-3} \, \text{s}^{-1}$ strain rate at 300 °C; (b) the experimental and predicted values of the maximum serration amplitude at each temperature under the condition of a strain rate of $1 \times 10^{-3} \, \text{s}^{-1}$. (c) The plot of Dp /Dl vs T/Tm for silver and CoNiV alloys; comparison of the amplitudes of stress rise and drop at different temperatures at $1 \times 10^{-3} \, \text{s}^{-1}$, (d) 300 °C, (e) 350 °C, (f) 400 °C.

where $\dot{\varepsilon}_1$ is the maximum strain rate during a stress drop and $\dot{\varepsilon}_2$ is the initial strain rate.

According to the simulation results of Hu et al., 29 $c_1 \dot{\varepsilon} \sigma_{dsa}$ is much larger than $c_2\{\exp[(M-\sigma_{dsa})/c_3]-1\}$. Hence, Eq. (2) can be simplified as

$$\dot{\sigma}_{dsa} = -c_1 \dot{\varepsilon} \sigma_{dsa}. \tag{4}$$

Solving the ordinary differential equation shown in Eq. (4), σ_{dsa} can be obtained as

$$\sigma_{dsa} = \exp\left(-\frac{1}{2}c_1\dot{\varepsilon}^2\right) + C. \tag{5}$$

Since $-(1/2)c_1\dot{\varepsilon}^2$ is small enough (less than 10^{-3}), it can be approximated to be close to 0. According to the Taylor expansion, ignoring higher-order terms, Eq. (5) can be approximated as

$$\sigma_{dsa} = -\frac{1}{2}c_1\dot{\varepsilon}^2 + C'. \tag{6}$$

Therefore, Eq. (3) can be further expressed as

$$\Delta \sigma = 2s_{in} \ln(\dot{\varepsilon}_1/\dot{\varepsilon}_2) + c_1|_2^2 - \dot{\varepsilon}_1^2|. \tag{7}$$

Substituting the maximum instantaneous strain rate into Eq. (7) can predict the maximum stress drop when considering above interactions.

From the insets in Figs. 1(a)-1(c), it is evident that the magnitude of the stress drop is not only affected by the strain rate, but also the temperature makes a significant contribution. In order to explore other factors affecting the serrated flow, the deformation structures after tension were examined. The bright-field image of TEM is exhibited in Fig. 5(a). The profuse deformation twins are available with a nano-scale spacing, and many dislocations are regularly accumulated near the deformation twins. It indicates that the barriers to mobile dislocations stem from deformation twins as well as solute atoms or precipitated phases. With straining, the mobile dislocations gradually accumulate under the obstacles of the deformation twins. When the strain energy is enough to allow the mobile dislocations to escape from the obstacles, the stress suddenly drops to form serrations. Thus, the model of Eq. (7) needs to be further modified to couple the influence of deformation twins. As shown in Figs. 4(d)-4(f), the total amplitude ratio of stress drop and stress rise at different temperatures is about 0.96%, which corresponds to a single serration, the magnitude of the stress rise and drop are approximately equal. As a result, the increase in the stress caused by twining strengthening can be used to approximately replace the decrease in the stress caused by dislocations breaking away from twins. According to the Hall-Petch relationship³⁰ from the resistance of the boundary slip, the twinning strengthening can be expressed as

$$\Delta \sigma_T = K_T \lambda^{-1/2},\tag{8}$$

where K_T is the Hall-Petch slope during twin deformation, and λ is the twinning space. Combining Eqs. (7) and (8), the prediction of revised stress-drop can be obtained as follows: $\Delta \sigma = 2s_{in}\ln(\dot{\varepsilon}_1/\dot{\varepsilon}_2) + c_1|\dot{\varepsilon}_2^2 - \dot{\varepsilon}_1^2| + K_T\lambda^{-1/2}$. We substitute relevant parameters to calculate the maximum stress drop from the stressstrain curves. As shown in Fig. 4(b), the predicted value at each temperature is slightly higher than the experimental one, and the errors are 7.2%, 9.6%, and 9.2%, respectively, indicating that the established modified model can accurately predict the maximum serration amplitude, i.e., the failure threshold.

It is extremely challenging to further predict the strain when the maximum serration occurs since the strain values are within the range of 0−1, and small changes in parameters may cause larger error. \mathfrak{L} Consequently, statistics on the serration-related parameters from the $\frac{Q}{Q}$ stress–strain curves are required. The complementary cumulative distribution functions (CCDFs) for the magnitudes of the amplitude of stress drops under different temperatures are plotted in Figs. 6 and 7. If the stress drop is less than 0.1 MPa,³¹ it is considered to be caused by mechanical vibrations and will not be counted in statistics. The ECDFs is $C(S, T) = (1 - T/T_c)^{-(\kappa - 1)/\sigma} C'[S(1 - T/T_c)^{1/\sigma}]^{.2}$ Here, $S(1 - T/T_c)^{1/\sigma}$ is an independent variable, and $C'[S(1 - T/T_c)^{1/\sigma}]$ is a universal scaling function. κ and $1/\sigma$ are the constants in meanfield theory, 33 and T_c is a critical constant of the curve fitting. The largest expected avalanche size, $S_{max}(T)$, grows with the

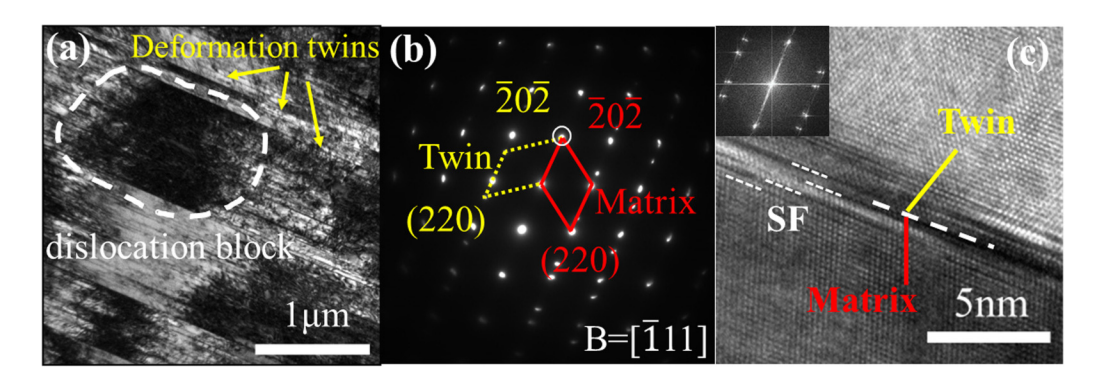


FIG. 5. TEM microstructure of the CoNiV MEA. (a) TEM image of a brightfield image of a sample after a 400 °C tensile test; (b) selected-area diffraction (SAD) patterns of twins; (c) high-angle annular dark-field (HAADF) image and fast Fourier transform (FFT) diagram of twins (inset).

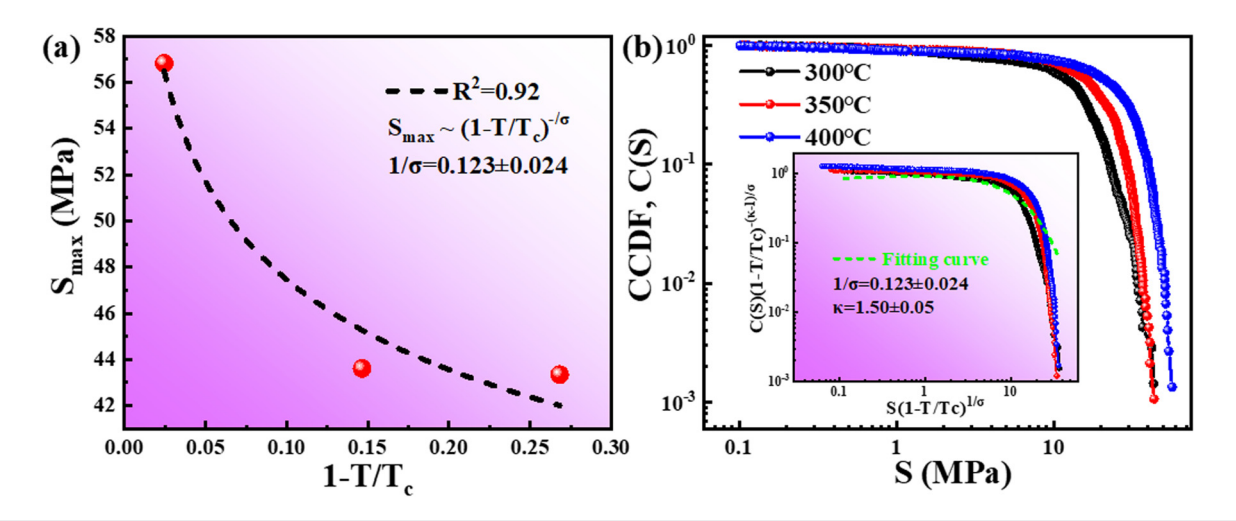


FIG. 6. (a) The fitting results of the experimental failure threshold S_{max} and temperature T, and (b) complementary cumulative distribution function of temperature with strain rates of $5 \times 10^{-4} \, \text{s}^{-1}$

temperature as $S_{\rm max}(T) \sim (1-T/T_c)^{-1/\sigma}$. According to the fitting results of Figs. 6(a) and 7(a), the equation can be obtained as

$$S_{\text{max}}(T) = C(1 - T/T_c)^{-1/\sigma},$$
 (9)

where *C* is the fitting constant.

From Figs. 6(b) and 7(b), $C(S, T)(1 - T/T_c)^{-(\kappa-1)/\sigma}$ vs $S(1-T/T_c)^{1/\sigma}$ for temperature-varied distributions was plotted. The normalized curve can be well fitted by a power-law distribution function and a squared exponential decay function $C(x) = \alpha x^{-\beta} \exp[-(x/x_c)^2]^{.34}$ Thus, the relationship between the distribution function of the serrations amplitude and the temperature is established, which can be used to further predict the distribution characteristics of the serration amplitude at other

Due to the sluggish diffusion in multicomponent HEAs/ MEAs, the explanation of the PLC mechanism in traditional alloys cannot simply be applied to HEAs. The in situ pinning mechanism with solute atoms by local diffusion in dislocation cores is more suitable for the CoNiV MEAs in this study, since there is an interaction between the solutes and dislocations. In order to reduce the total energy, solute atoms always tend to diffuse into dislocations and cause segregation or atmosphere due to strain release and chemical bonding effects. Therefore, in the current ternary alloys, &

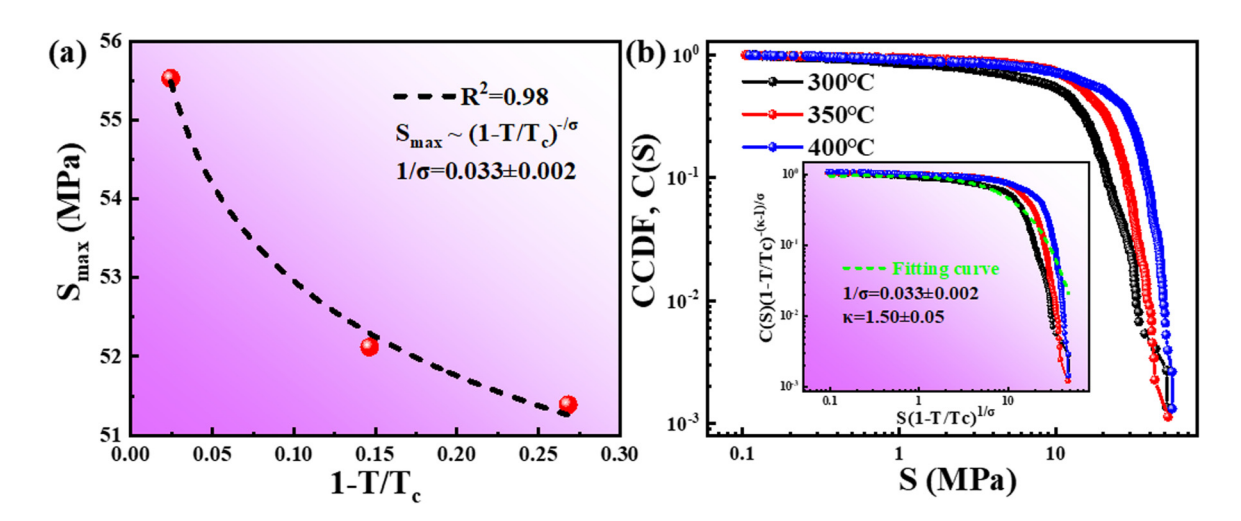


FIG. 7. (a) The fitting results of the experimental failure threshold S_{max} and temperature T_{ij} and (b) complementary cumulative distribution function of temperature with strain rates of $1 \times 10^{-3} \,\mathrm{s}^{-1}$

larger atoms, V (r = 1.34 Å), will tend to segregate into or near the lower part of the edge dislocation core, while Co (r = 1.25 Å) and Ni (r = 1.25 Å) in or near the upper part of the edge dislocation core. There are atomic-size differences among V atoms and the other two kinds of atoms, which is easy to generate a strain field around the solute atoms. A high concentration of displacementsolute atoms will have a high density of locally strained lattice sites. The formation of solute-atom segregation or atmosphere around the strain source causes in situ pinning. Figure 4(c) exhibits the plot of $\ln(D_p/D_l)$ vs T/T_m for silver $(D_p$ and D_l indicating the diffusion coefficient of the solute atom in the dislocation core and the diffusion coefficient in the crystal lattice, respectively).³⁵ The equation can be obtained by a linear fitting: $ln(D_p/D_l) = C_1(T/T_m) + C_2$. Considering that D_p / D_l is dimensionless, it is affected by the alloy type. Since both silver and CoNiV alloys are FCC lattices, the ln (Dp/Dl) and $T/T_{\rm m}$ trends of CoNiV alloys can be plotted as shown in Fig. 4(c). $T_{\rm m}$ = 1250 °C of CoNiV alloys was obtained by simulating the phase diagram in the supplementary material. The dislocation-nuclear diffusion coefficient relationship in the CoNiV MEA can be expressed as

$$D_p = D_l \exp(AT + B). \tag{10}$$

According to the Arrhenius equation, Eq. (10) will be transformed into

$$D_p = D_0 \exp(AT + B - Q/RT), \tag{11}$$

where D_0 is the pre-exponential factors and Q is the activation energy.

The atomic-diffusion process can be considered as a random jump process. According to the relationship between the diffusion coefficient and the average atomic jumping rate: $D=(1/6)\Gamma\alpha^2$, the time expression of the atomic diffusion can be calculated as ³⁶

$$t_p = 1/\Gamma_p = \alpha^2/6D_p, \tag{12}$$

where α is the plane distance of the position before and after atom diffuses. The calculated atomic diffusion time can be considered to be the DSA time, t_a , in the PLC effect.

The PLC theory holds that the PLC effect occurs when the waiting time $t_{\rm w}$ is equal to the DSA time $t_{\rm a}$. The waiting time, $t_{\rm w}$, can be expressed as 37

$$t_{w} = \rho Lb/\dot{\varepsilon},\tag{13}$$

where ρ is the mobile dislocation density, L is the obstacle spacing, b is the Burgers vector, and $\dot{\varepsilon}$ is the strain rates. For the tensile test at the same conditions, the obstacle spacing, Burgers vector, and strain rates can be approximately regarded as constants. In contrast, the dislocation density will be changed significantly with straining. It is assumed that the dislocation density and strain satisfy an exponential relationship of $\rho = N\varepsilon^{\beta}$ (N and β being constants), which can be obtained by fitting the experimental data. In view of the fact that the relationship between the dislocation density and strain of CoNiV MEAs has not been studied, and CoNiV MEAs, as a subseries alloy of Cantor alloy, have dislocation density close to that of

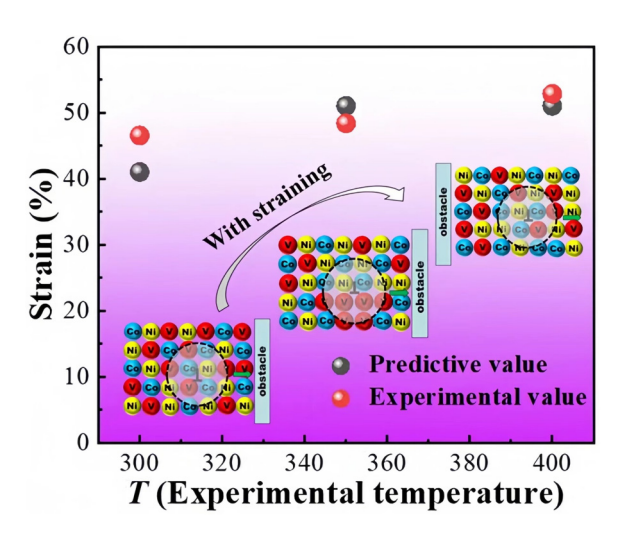


FIG. 8. Predicted and experimental values of strains when the largest serration appears and a schematic diagram of the mechanism of *in situ* pinning.

the Cantor alloy. In this study, we select the relevant data of CrMnFeCoNi HEAs reported by Naeem *et al.*³⁹ and fit the relationship between dislocations and strain rates as $\rho=3.3\times10^{14}\varepsilon^{0.84}$. Substituting the dislocation-density relationship into Eq. (13), it is obtained as

$$t_w = 3.3 \times 10^{14} \varepsilon^{0.84} Lb/\dot{\varepsilon}. \tag{14}$$

Equations (9), (11), (12), and (14) form a closed solution space. When the maximum serration occurs, the tensile strain can be obtained. It is worth noting that the pre-exponential factors, D_0 , in Eq. (11) is significantly different for various elements. In other words, for multi-principal alloys, the special elements play a leading role in the PLC effect under various conditions. For instance, through the calculation, it is found that at 300-400 °C, the Co and Ni atoms play a leading role in the CoNiV MEA, while the diffusion rate of V atoms is too low to form an effective pin. At the strain rate of 5×10^{-4} s⁻¹, the calculated and experimental results for the strain corresponding to the largest avalanche size in the CoNiV alloy at different temperatures are exhibited in Fig. 8. As the temperature increases, the theoretical value is getting closer and closer to the experimental value. The possible reason is that the diffusion speed of atoms is slower at low temperatures, and the pinning is more complicated. At higher temperatures, the rearrangement of Co and Ni atoms is likely to form more effective pinning, making the predicted value closer to the experimental value. If the temperature further increases, both the type and number of activated atoms increase, the types of elements involved in pinning dislocations also increase, the trend of Fig. 8 cannot be used to further predict the maximum serration amplitude related parameters at higher temperatures. In future work, the studies of serration behavior at higher temperatures are needed.

IV. CONCLUSIONS

During the tensile tests of the CoNiV MEA at different strain rates and temperatures, the serration type change conforms to the serration characteristics of traditional alloys. With the increase of the temperature and the decrease of the strain rate, the serration type changes from types A to B, and then to C. The failure-threshold prediction model is successfully established to predict the maximum serration amplitude upon tensile loading. Based on the known maximum serration amplitude, combined with the mean-field theory and in situ pinning model, the corresponding engineering strain value can be well predicted.

SUPPLEMENTARY MATERIAL

See the supplementary material for related charts and graphs mentioned in the article.

ACKNOWLEDGMENTS

J.Q.W. would like to acknowledge financial support of the National Natural Science Foundation of China (No. 52271110). H.Y.J. would like to acknowledge financial support of Key Research Development Program of Shanxi Province (No. 202102050201008). Z.W. very much appreciates financial support of the National Natural Science Foundation of China (No. 52201188). P.K.L. is very grateful for the support from (1) the National Science Foundation (Nos. DMR-1611180 and 1809640) with the program directors, Dr. Judith Yang, Dr. Gary Shiflet, and Dr. Diana Farkas and (2) the U.S. Army Research Office Project (Nos. W911NF-13-1-0438 and W911NF-19-2-0049) with the program managers, Dr. M. P. Bakas, Dr. S. N. Mathaudhu, and Dr. D. M. Stepp.

AUTHOR DECLARATIONS

Conflict of Interest

The authors declare no conflict of interests.

Author Contributions

Rong Hao: Methodology (equal). Guanhao Liu: Conceptualization (equal). Zhong Wang: Data curation (equal). Huijun Yang: Formal analysis (equal). Peter K. Liaw: Funding acquisition (equal). Junwei Qiao: Methodology (equal).

DATA AVAILABILITY

The data that support the findings of this study are available from the corresponding author upon reasonable request.

REFERENCES

- ¹Y. I. Golovin, V. Ivolgin, V. Khonik, and K. Kitagawa, Scr. Mater. 45(8), 947-952 (2001).
- ²Y. Zhang, J. P. Liu, S. Y. Chen, X. Xie, P. K. Liaw, K. A. Dahmen, J. W. Qiao, and Y. L. Wang, Prog. Mater. Sci. 90, 358-460 (2017).
- ³Z. Jiang, Q. Zhang, H. Jiang, Z. Chen, and X. Wu, Mater. Sci. Eng. A 403(1-2), 154-164 (2005).

- ⁴A. Yilmaz, Sci. Technol. Adv. Mater. 12(6), 063001 (2011).
- ⁵R. Mulford and U. Kocks, Acta Metall. 27(7), 1125–1134 (1979).
- ⁶P. McCormick and C. Ling, Acta Metall. Mater. 43(5), 1969–1977 (1995).
- ⁷S. D. Mesarovic, J. Mech. Phys. Solids **43**(5), 671–700 (1995).
- ⁸J. W. Yeh, S. J. Lin, T. S. Chin, J. Y. Gan, S.-K. Chen, T. T. Shun, C.-H. Tsau, and S. Y. Chou, Metall. Mater. Trans. A 35, 2533-2536 (2004).
- ⁹J. W. Yeh, S. K. Chen, S. J. Lin, J. Y. Gan, T. S. Chin, T. T. Shun, C. H. Tsau, and S. Y. Chang, Adv. Eng. Mater. 6(5), 299-303 (2004).
- ¹⁰T. K. Chen, T. T. Shun, J. W. Yeh, and M. S. Wong, Surf. Coat. Technol. 188-189, 193-200 (2004).
- ¹¹P. K. Huang, J. W. Yeh, T. T. Shun, and S. K. Chen, Adv. Eng. Mater. 6(12), 74-78 (2004).
- 12Y. Zhang, T. T. Zuo, Z. Tang, M. C. Gao, K. A. Dahmen, P. K. Liaw, and Z. P. Lu, Prog. Mater. Sci. 61, 1-93 (2014).
- ¹³D. B. Miracle and O. N. Senkov, Acta Mater. **122**, 448–511 (2017).
- ¹⁴P. Shi, R. Li, Y. Li, Y. Wen, Y. Zhong, W. Ren, Z. Shen, T. Zheng, J. Peng, and X. Liang, Science 373(6557), 912-918 (2021).
- 15Q. Pan, L. Zhang, R. Feng, Q. Lu, K. An, A. C. Chuang, J. D. Poplawsky, P. K. Liaw, and L. Lu, Science 374(6570), 984-989 (2021).
- 16_{M. C. Gao, C. S. Carney, ÖN Doğan, P. D. Jablonksi, J. A. Hawk, and} D. E. Alman, Jom 67(11), 2653-2669 (2015).
- ¹⁷J.-W. Yeh, Jom **65**(12), 1759–1771 (2013).
- 18 H. Y. Diao, R. Feng, K. A. Dahmen, and P. K. Liaw, Curr. Opin. Solid State Mater. Sci. 21(5), 252-266 (2017).
- 19 A. S. Tirunilai, T. Hanemann, K. P. Weiss, J. Freudenberger, M. Heilmaier, and A. Kauffmann, Acta Mater. 200, 980-991 (2020).
- ²⁰M. Naeem, H. He, F. Zhang, H. Huang, S. Harjo, T. Kawasaki, B. Wang, S. Lan, Z. Wu, and F. Wang, Sci. Adv. 6(13), eaax4002 (2020).
- ²¹M. Naeem, H. He, S. Harjo, T. Kawasaki, W. Lin, J.-J. Kai, Z. Wu, S. Lan, and X.-L. Wang, Acta Mater. 221, 117371 (2021).
- 22W. A. Curtin, D. L. Olmsted, and L. G. Hector, Jr., Nat. Mater. 5(11), 875–880 ω (2006).
- ²³K. Y. Tsai, M. H. Tsai, and J. W. Yeh, Acta Mater. 61(13), 4887–4897 (2013).
- ²⁴C.-W. Tsai, C. Lee, P.-T. Lin, X. Xie, S. Chen, R. Carroll, M. LeBlanc, P. A. W. Brinkman, P. K. Liaw, K. A. Dahmen, and J.-W. Yeh, Int. J. Plast. 122, 24 212-224 (2019).
- **25**P. Rodriguez, Bull. Mater. Sci. **6**, 653–663 (1984).
- ²⁶Y. Yang, Z. Li, W. Zhang, Y. Ma, Q. Xiong, W. Li, S. Chen, and Z. Wu, Scr. No. Mater. 211, 114504 (2022).
- 27Y. S. Luo, Z. Wang, J. Eckert, and J. W. Qiao, J. Appl. Phys. 129, 155109 (2021).
- ²⁸J. Brechtl, S. Chen, C. Lee, Y. Shi, and P. K. Liaw, Metals 10(8), 1101 (2020).
- ²⁹Q. Hu, Q. Zhang, P. Cao, and S. Fu, Acta Mater. **60**(4), 1647–1657 (2012).
- 30 H. Bahmanpour, K. M. Youssef, J. Horky, D. Setman, M. A. Atwater, M. J. Zehetbauer, R. O. Scattergood, and C. C. Koch, Acta Mater. 60(8), 3340-3349 (2012).
- 31 J. Li, J. F. Fan, Z. Wang, Y. C. Wu, K. A. Dahmen, and J. W. Qiao, Intermetallics 116, 106637 (2020).
- 32 J. Antonaglia, X. Xie, G. Schwarz, M. Wraith, J. Qiao, Y. Zhang, P. K. Liaw, J. T. Uhl, and K. A. Dahmen, Sci. Rep. 4, 4382 (2014).
- 33K. A. Dahmen, Y. Ben-Zion, and J. T. Uhl, Phys. Rev. Lett. 102(17), 175501 (2009).
- 34G. Wang, K. C. Chan, L. Xia, P. Yu, J. Shen, and W. H. Wang, Acta Mater. 57(20), 6146-6155 (2009).
- 35P. Shewmon, Diffusion in Solids (McGraw-Hill, New York, 1963).
- 36D. Porter, Phase Transformations in Metals and Alloys (Chapman & Hall,
- 37 G. Saha, P. McCormick, and P. R. Rao, Mater. Sci. Eng. 62(2), 197–203 (1984).
- 38 R. K. Ham and D. Jaffrey, Philos. Mag. 15(134), 247–256 (1967).
- 39 M. Naeem, H. He, S. Harjo, T. Kawasaki, F. Zhang, B. Wang, S. Lan, Z. Wu, Y. Wu, Z. Lu, C. T. Liu, and X.-L. Wang, Scr. Mater. 188, 21-25 (2020).